Admittance Study of Grid-Connected VSCs for Harmonic Oscillatory Instabilities

Luis Sainz[1*], Lluis Monjo[2], Marc Cheah-Mane [1], J. Liang[3], O. Gomis-Bellmunt[1], E. Prieto-Araujo[1]

[1] Department of Electrical Engineering, ETSEIB-UPC, Av. Diagonal 647, 08028 Barcelona, Spain
[2] Department of Industrial and Design System Engineering, Univ. Jaume I, Av. de Vicent Sos Baynat, s/n, 12071 Castelló de la Plana, Spain
[3] School of Engineering, Cardiff University, CF24 3AA, Cardiff, U.K
[*] sainz@ee.upc.edu

Abstract: Voltage source converters (VSCs) can reduce damping of grid-connected VSC systems at harmonic resonances, leading to system instability. The conductance of the VSC admittance can be shaped selecting appropriate VSC parameter values in order to increase VSC damping at poorly damped harmonic resonances and ensure system stability. This paper extends existing findings and makes contributions in this direction. Analytical expressions of the positive- and negative-sequence VSC conductance are presented to study exhaustively the impact of VSC parameters on harmonic oscillatory instabilities. Two applications, i.e., a traction system and an offshore wind power plant, are used to show the contribution of this paper. The analytical study is validated from PSCAD/EMTDC time-domain simulations.

1. Introduction

Voltage source converters (VSCs) are employed in a number of electric system applications such as high-voltage dc transmission, renewable energy conversion, energy storage, flexible ac transmission and ac traction. They are commonly referred to as grid-connected VSCs [1], [2]. VSCs improve power system controllability but may also cause oscillatory instabilities when interacting with resonances. These instabilities can be classified into two categories depending on their frequency range: near-synchronous oscillatory instabilities (from 10 to 100 Hz) due to inner and outer controls, and harmonic oscillatory instabilities (from 0.1 to 2 kHz) due to VSC time delay and current control (CC) dynamics [3], [4]. Harmonic oscillatory instabilities are found in several VSC applications such as HVDC grids [3], [5], wind power plants (WPPs) [6] and ac traction systems [7] – [13]. In traditional power systems, damping of resistive loads is sufficient to prevent these instabilities but they may arise in systems with large penetration of grid-connected VSCs and few resistive and rotating mass loads [3], [7].

Frequency domain methods are used to study stability with fewer calculations and data than state space eigenvalue analysis [14]. The passivity-based method ensures closed-loop system stability if the real part of each subsystem is non-negative for all frequencies [4], [15] – [18]. Other frequency domain methods consider the contribution of each subsystem to system stability. One of them is the impedance-based stability approach, which determines the phase margin of the grid-connected VSC system from the phase of the grid and VSC impedances at frequencies where their magnitudes are equal [1], [19]. An alternative method is the positive-net-damping (PND) stability criterion, which determines the damping of the grid-connected VSC at system resonance frequencies [5], [14], [20]. The PND stability criterion is more practical for system stability assessment than the impedance-based stability criterion because damping is related to system resistances and is analytically determined more easily than the phase margin [14]. As an example, the numerical study in [21] on the impact of closed-loop CC bandwidth, grid voltage low-pass filter bandwidth and grid short-circuit ratio on near-synchronous resonance instabilities may be performed analytically from VSC damping.

Grid-connected VSC stability is commonly assessed from VSC circuit and control design assuming that the grid impedance is fixed [6]. In general, instabilities are mainly caused by poorly damped resonances related to poorly damped poles of the system. In the literature, different active damping methods are shown to improve them. They propose control loop modifications based on the passivity-based method [4], [15] – [17] and the impedance-based stability criterion [22] – [24]. These changes are intended to reshape the VSC impedance (or admittance) to increase VSC damping, i.e., obtaining a nonnegative value of its resistance (or conductance) in order to damp resonances. However, these approaches may have undesired effects on control performance, such as interactions with other converter control loops or other VSCs connected to the same grid, and an influence on grid resonances [3], [22], [23]. A few studies also analyze the impact of control parameters on the VSC impedance (or admittance) to increase VSC damping with a suitable selection of their values [4], [15], [17], [21]. In [4], [15] and [17], the VSC admittance is determined and VSC damping at harmonic resonance frequencies depends on VSC time delay, closed-loop CC bandwidth and grid voltage low-pass filter bandwidth. Nevertheless, only the impact of VSC time delay on VSC damping is analyzed because it is considered that the VSC works in normal operation mode with small bandwidth values of the grid voltage low-pass filter. Under this assumption, the influence of closed-loop CC bandwidth and grid voltage low-pass filter bandwidth can be simplified. In [21], the influence of closed-loop CC bandwidth, grid voltage low-pass filter bandwidth and grid strength on near-synchronous resonance

instabilities is numerically investigated. VSC time delay is approximated at the near-synchronous frequency range as a first-order transfer function.

The main goal of this paper is to provide a complete and comprehensive overview of the influence of VSC parameters on VSC damping at harmonic resonance frequencies. Expressions of the positive- and negative-sequence VSC conductance are presented, and VSC damping at harmonic resonance frequencies is analytically and numerically investigated. According to this study, previous findings in the literature are analytically clarified and the following contributions related to VSC damping are derived from the study:

- Existing studies are extended to all involved VSC control parameters considering normal and transient operation mode (i.e., considering any value of the grid voltage low-pass filter bandwidth).
- Practical analytical relations between VSC control parameters and boundary frequencies of the VSC negative-damping region are proposed to determine whether the harmonic resonance frequencies are in this region, compromising system stability.
- Simple but reliable analytical expressions for determining the limits of VSC parameters to ensure system stability are proposed. These expressions allow the distance between the design values of these parameters and the stability limits to be assessed.
- Recommendations to determine the influence of VSC control parameters on the boundary frequencies of the VSC negative-damping region and grid-connected VSC stability are made.

A traction system and an offshore WPP are studied to illustrate the paper contributions. PSCAD/EMTDC simulations are used to validate the application results.

2. Grid-Connected VSC Stability

Harmonic resonances between 100 Hz and 2 kHz may cause system instabilities as a result of the negative-conductance response of grid-connected VSCs [3], [4], [24]. These harmonic oscillatory instabilities are assessed in the frequency domain by means of the impedance-based characterization of grid-connected VSCs [1], [14] – [19]. This representation allows the causes of the negative-conductance response of VSCs and interactions with harmonic resonances to be looked into. Simple networks with one VSC are commonly analyzed to obtain useful conclusions about the influence of VSC parameters on poorly damped resonances compromising system stability [4], [15], [19], [22]. These conclusions can be further used to understand interactions in large systems with several VSCs.

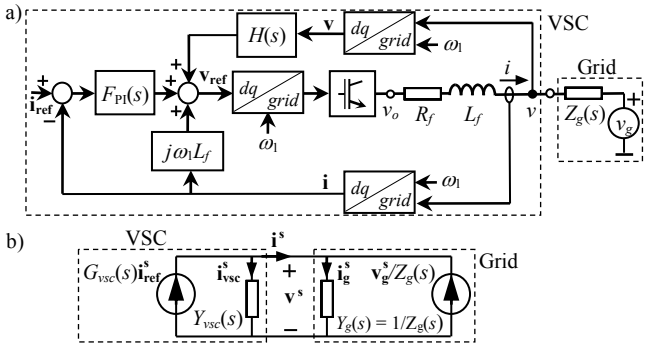

Fig. 1. *System model:*
(a) Grid-connected VSC system. **(b)** Impedance-based equivalent circuit.

2.1. Impedance-based representation of grid-connected VSCs

A grid-connected VSC system is illustrated in Fig.1(a). The VSC is represented by its block and circuit diagram, and the grid is characterized by the Thevenin circuit with v_g and $Z_g(s)$. VSC control is represented as a PI-based CC in *dq*-frame, where complex space voltages and currents are denoted in boldface as $\mathbf{v} = v_d + j \cdot v_q$ and $\mathbf{i} = i_d + j \cdot i_q$ [15]. These vectors are obtained from the *dq*-transformation of the single- [9] or three-phase- [2] grid components *v* and *i*. The outer control loop dynamics is neglected because these loops are slower than the inner CC loop and their low bandwidths do not affect the harmonic oscillatory instabilities. This dynamics may affect VSC non-passivity at near-synchronous frequencies [4], [15], [18], [21] but are beyond the scope of the study.

2.1.1 Grid-connected VSC model: The VSC model with complex space vectors in *dq*-frame is obtained from the current dynamics,

$$\mathbf{v_o} = (R_f + L_f s + jL_f \omega_1)\mathbf{i} + \mathbf{v}, \tag{1}$$

and the VSC voltage reference,

$$\mathbf{v_{ref}} = F_{\mathrm{PI}}(s)\left(\mathbf{i_{ref}} - \mathbf{i}\right) + jL_f \omega_1 \mathbf{i} + H(s)\mathbf{v}, \tag{2}$$

where $\mathbf{v}$ and $\mathbf{i}$ are the grid voltage and current, $\mathbf{v_o}$ is the VSC output voltage, $\mathbf{i_{ref}}$ is the VSC current reference and $\omega_1 = 2\pi \cdot f_1$ is the grid angular frequency. The PI of the CC and the grid voltage low-pass filter are considered as

$$F_{\mathrm{PI}}(s) = k_p + \frac{k_i}{s} \qquad H(s) = \frac{\alpha_f}{s + \alpha_f}, \tag{3}$$

where k_p and k_i are the PI control gains and $\alpha_f = 2\pi f_f$ is the grid voltage low-pass filter bandwidth.

The voltage $\mathbf{v_o}$ is obtained from $\mathbf{v_{ref}}$ by means of the VSC time delay T_d as [15], [14], [18]:

$$\mathbf{v_o} = D(s)\mathbf{v_{ref}} \qquad D(s) = e^{-sT_d}. \tag{4}$$

Finally, the relation between $\mathbf{v}$ and $\mathbf{i}$ is obtained combining (1), (2) and (4) as

$$\mathbf{i} = G_{vsc}(s)\mathbf{i_{ref}} - Y_{vsc}(s)\mathbf{v}, \tag{5}$$

where $G_{vsc}(s)$ is the VSC closed-loop transfer function and $Y_{vsc}(s)$ is the VSC admittance,

$$G_{vsc}(s)=\frac{D(s)F_{\mathrm{PI}}(s)}{R_f+L_f s+jL_f\omega_1+D(s)(F_{\mathrm{PI}}(s)-jL_f\omega_1)}$$
$$Y_{vsc}(s)=\frac{1-D(s)H(s)}{R_f+L_f s+jL_f\omega_1+D(s)(F_{\mathrm{PI}}(s)-jL_f\omega_1)}. \quad (6)$$

The VSC can be characterized as a Norton source (5) and the impedance-based equivalent circuit of the grid-connected VSC system in Fig. 1(a) is represented as in Fig. 1(b). This VSC model is not valid for frequencies above the Nyquist frequency because the delay model does not consider the effect of the sampling process [18]. In order to represent the VSC and grid in the same frame, the VSC model (5) is modified from *dq*- to $\alpha\beta$-frame by means of the rotation $s \rightarrow s - j\omega_1$ whereas the grid model in *abc*-frame is not modified because it is the same as in $\alpha\beta$-frame [4], [16]. The circuit in Fig. 1(b) is characterized as a closed-loop system [1], [15], [16] by considering the current sources and the grid voltage:

$$\mathbf{v^s}=Z_t(s)\left(G_{vsc}(s)\mathbf{i^s_{ref}}+\frac{\mathbf{v^s_g}}{Z_g(s)}\right)$$
$$Z_t(s)=\frac{1/Y_g(s)}{1+Y_{vsc}(s)/Y_g(s)}, \quad (7)$$

which is rewritten as

$$F(s)=Z_t(s)=\frac{M(s)}{1+L(s)} \qquad L(s)=M(s)N(s), \quad (8)$$

where $L(s)$ is the loop transfer function and $M(s) = 1/Y_g(s)$ and $N(s) = Y_{vsc}(s)$ are the open-loop and feedback transfer functions.

2.1.2 VSC parameter values: The range of parameters related to VSC conductance response at harmonic resonances must be determined to determine their influence on stability. According to the VSC admittance in (6), VSC time delay and CC dynamics (i.e., closed-loop CC bandwidth and grid voltage low-pass filter bandwidth) are identified as main parameters with an effect on VSC conductance response at the harmonic frequency range [4], [15], [17], [23].

Time delay may cause VSC non-passivity approximately below the converter switching frequency [4], [15] – [17]. Time delay in VSCs with PWM depends on the sampling technique [4], [6]. In the double-update (d-u) PWM technique, the sampling frequency f_s is twice the VSC switching frequency f_{sw} (i.e., $f_s = 2f_{sw}$) and time delay is 1.5 times the sampling period $T_s = 1/f_s$ (i.e., $T_d = 1.5 \cdot T_s$). This is due to the CC computation time, which may reach a maximum value of T_s, and the average PWM time delay, which is at least $0.5T_s$. In the single-update (s-u) PWM technique, sampling frequency is set equal to VSC switching frequency (i.e., $f_s = f_{sw}$) and time delay is equal to the sampling period (i.e., $T_d = T_s$). This is due to the CC computation time, which may reach a maximum value of $0.5T_s$, and the average PWM time delay, which is at least $0.5T_s$. Therefore, time delay can be expressed as a factor q_d of the VSC switching period $T_{sw} = 1/f_{sw}$ [15]:

$$T_d = q_d \cdot T_{sw} \quad q_d \in \begin{cases} [0.25 \ldots 0.75] & \text{in d-u PWM tech.} \\ [0.5 \ldots 1] & \text{in s-u PWM tech.} \end{cases} \quad (9)$$

The minimum values of T_d in (9) for the double- and single-update PWM techniques can be obtained by reducing CC computation time to zero [4], i.e., by reducing the factor q_d. Although T_d also depends on the VSC switching frequency f_{sw}, it is not a feasible parameter for reducing T_d because the design of the VSC output filter L_f and the calculation of PI control gains are based on it. Moreover, a change in f_{sw} affects VSC switching losses.

The CC dynamics may also influence VSC non-passivity [4], [21]. Based on [15], the design of the PI control (3) results in

$$k_p = \alpha_c L_f \qquad k_i = \alpha_c R_f, \quad (10)$$

where α_c is the closed-loop CC bandwidth. According to [4], [15], its recommended value is

$$\alpha_c \le 0.2 \cdot \omega_{sw} = 0.2 \cdot 2\pi f_{sw}. \quad (11)$$

The bandwidth α_f in (3) is also related to VSC non-passivity [21]. A small α_f should be used to obtain a tight VSC non-passivity region caused by outer control loops at near-synchronous frequencies [4], [21]. A large α_f is needed to enhance dynamics during fast transients [2], [15], [16], [21]. Thus, according to [16], the filter design results in

$$\alpha_f = \begin{cases} \alpha_{fn} \le 0.1\alpha_c & \text{in normal operation mode} \\ \alpha_{ft} \ge \alpha_c & \text{in transient operation mode,} \end{cases} \quad (12)$$

where the VSC mode is modified according to measurements of grid variables (e.g., in case of fault). VSC dynamics during fast transients can also be improved by different PWM methods [25].

2.1.3 Analysis of grid-connected VSC stability: The circuit in Fig. 1(b) allows stability to be analyzed from the poles of $F(s)$ (8). The Nyquist and Bode diagrams are also common tools to determine stability in the frequency domain [1], [19] – [22]. However, both diagrams study the loop transfer function $L(j\omega)$ $-\infty < \omega < \infty$, but the influence of the grid and VSC on system stability cannot be analyzed separately. The impedance-based and PND stability criteria assess the contribution of each subsystem to the positive- ($s = j\omega$, $\omega > 0$) and negative- ($s = -j\omega$, $\omega > 0$) sequence components. The impedance-based stability criterion determines the phase margin as the phase difference ($\gamma_m = \arg\{Y_{vsc}(\pm j\omega)\} - \arg\{Y_g(\pm j\omega)\}$, $\omega > 0$) between the VSC and grid admittances at frequencies where their magnitudes are equal. This frequency approximately matches the frequency of the harmonic resonance between the VSC and grid admittances [1], [19] – [22]. The PND stability criterion determines system damping (i.e., $G(\pm\omega) = \mathrm{Re}\{Y_g(\pm j\omega) + Y_{vsc}(\pm j\omega)\}$, $\omega > 0$) at harmonic resonance

frequencies [14]. This criterion is a reformulation of the impedance-based stability criterion, where net damping at harmonic resonances is evaluated instead of phase margin for stability assessment (see Appendix). This enables analytical expressions to further investigate the impact of VSC parameters on stability to be obtained.

3. VSC Negative-Damping Region

The VSC negative-damping region defines stability conditions. The frequency range where the real part (conductance) of the VSC admittance is negative is used to characterize this region. Although stability may not be ensured if the VSC negative-damping region is shifted above the Nyquist frequency (i.e., just above the switching frequency f_{sw}, considering the double-update PWM technique) [18], it is accepted that a VSC positive-damping region from 250 Hz to the Nyquist frequency is sufficient to ensure stability in most practical situations [10]. Moreover, since the previous condition is difficult to satisfy [18], stability is practically achieved by ensuring that the harmonic resonance frequencies are not in the negative-damping region.

3.1. Study of the VSC negative-damping region

VSC admittances are expressed in the frequency domain for the positive- and negative-sequence *dq*-frame space vectors by setting $s = j\omega$ and $s = -j\omega$, $\omega > 0$ in (6) [1], [2], [22], [23]:

$$Y_{vsc}(\pm j\omega) = \frac{1 - D(\pm j\omega)H(\pm j\omega)}{R_f + jL_f(\omega_1 \pm \omega) + D(\pm j\omega)(F_{\mathrm{PI}}(\pm j\omega) - jL_f\omega_1)}, \quad (13)$$

where $F_{\mathrm{PI}}(\pm j\omega)$, $H(\pm j\omega)$ and $D(\pm j\omega)$ are written from (3) and (4) as

$$F_{\mathrm{PI}}(\pm j\omega) = k_p \mp j\frac{k_i}{\omega} \qquad H(\pm j\omega) = \frac{\alpha_f}{\alpha_f \pm j\omega}$$
$$D(\pm j\omega) = D_{r\pm}(\omega) + jD_{i\pm}(\omega) = \cos(\omega T_d) \pm j\sin(\omega T_d). \quad (14)$$

The conductance $G_{vsc}(\pm\omega) = \mathrm{Re}\{Y_{vsc}(\pm j\omega)\}$ can be numerically derived from (13) to study the influence of VSC parameters on system stability. However, (13) can be simplified if the filter resistance R_f and the integral gain k_i (10) are neglected due to their small value:

$$Y_{vsc}(\pm j\omega) \approx \frac{1 - D(\pm j\omega)H(\pm j\omega)}{L_f\left(j(\omega_1 \pm \omega) + D(\pm j\omega)(\alpha_c - j\omega_1)\right)}. \quad (15)$$

Then, an expression of $G_{vsc}(\pm\omega)$, which allows further analysis of system stability, is determined from (15) after several mathematical manipulations:

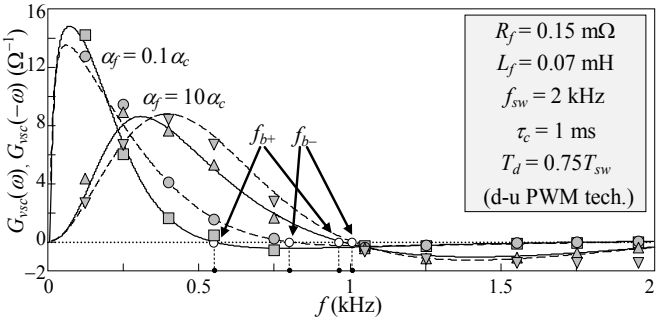

Fig. 2. *Real part of the positive- and negative-sequence VSC admittance. Continuous and dashed lines: Analytical expression (16) (*$G_{vsc}(\omega)$ *and* $G_{vsc}(-\omega)$*, respectively); Dots: PSCAD results.*

$$G_{vsc}(\pm\omega) \approx \frac{G^N_{vsc}(\pm\omega)}{G^D_{vsc}(\pm\omega)} = \frac{D_{r\pm}(\alpha_f + \alpha_c)\omega^2 + (D_{r\pm} - 1)\alpha_f(\alpha_f\alpha_c \pm \omega\omega_1) + D_{i\pm}(\alpha_f^2 - \omega\omega_1)\omega}{L_f(\omega^2 + \alpha_f^2)(\omega^2 + \alpha_c^2 - 2(\omega_1 \pm \omega)(D_{i\pm}\alpha_c + (D_{r\pm} - 1)\omega_1))}. \quad (16)$$

where the functions $D_{r\pm}(\omega)$ and $D_{i\pm}(\omega)$ (14) are denoted as $D_{r\pm}$ and $D_{i\pm}$ for simplicity. Fig. 2 compares the simplified expression of $G_{vsc}(\pm\omega)$ in (16) against PSCAD numerical results for $\alpha_f = 0.1\alpha_c$ (normal mode) and $\alpha_f = 10\alpha_c$ (transient mode) (12). PSCAD numerical results are obtained by injecting a superimposed perturbation into the VSC without any simplification and measuring the response of the VSC impedance at multiple frequency values. It can be noted that (16) provides an accurate approximation at harmonic resonance frequencies (i.e., above 100 Hz). The difference between the simplified expression in (16) and the PSCAD numerical results is mainly because of the PI control integral term k_i/s being neglected. As can be seen in Fig. 2, the VSC admittance has a negative damping region for frequencies higher than the boundary frequencies f_{b+} and f_{b-} corresponding to the positive- and negative-sequence, respectively. The damping region is not affected by the VSC outer control loops, whose dynamics is in the subsynchronous frequencies [4], [15], [21]. The frequencies f_{b+} and f_{b-} can be derived from

$$G^N_{vcs\pm}(\omega_{b\pm}) = 0 \quad (\omega_{b\pm} = 2\pi f_{b\pm}), \quad (17)$$

where $G^N{}_{vsc}(\pm\omega)$ in (16) is denoted as $G^N{}_{vsc\pm}(\omega)$. This is a nonlinear system that can be numerically solved by the Newton method and considering the approximate expressions of $f_{b\pm}$ in Section 3.2 as initial values.

It can be observed from the numerator in (16) that $f_{b\pm}$ depends on four VSC parameters [4], [15], [14]:

- The grid voltage low-pass filter bandwidth α_f.
- The VSC switching frequency f_{sw} and the factor q_d. The influence of f_{sw} and q_d is included in the time delay $T_d = q_d \cdot T_{sw}$ (9), which is part of the expressions of $D_{r\pm}$ and $D_{i\pm}$ (14).
- The closed-loop CC bandwidth α_c.

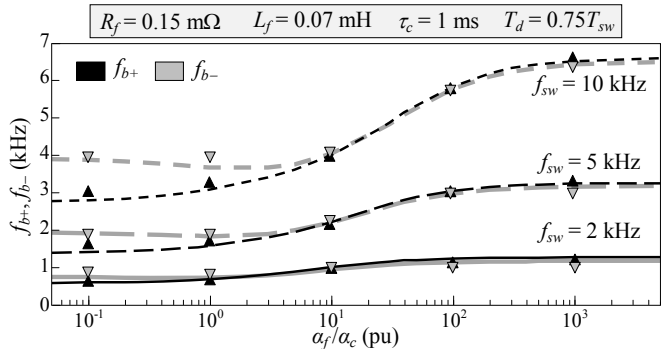

Fig. 3. *Influence of the VSC low-pass filter bandwidth on the boundary frequencies f_{b+} and f_{b-} of the VSC negative damping region. Lines: Analytical expression (17); Dots: PSCAD results.*

Note that the VSC admittances in (16) are in *dq*-frame and are expressed in $\alpha\beta$-frame by translating the frequency spectrum as $\omega \rightarrow \omega - \omega_1$ for positive-sequence and $\omega \rightarrow \omega + \omega_1$ for negative-sequence. According to this, the positive-sequence boundary frequency of the VSC negative-damping region in $\alpha\beta$-frame (and also in the grid-frame) is obtained as $f_{b+} + f_1$ and the negative-sequence boundary frequency is obtained as $f_{b-} - f_1$ [1], [22]. Fig. 3, Fig. 4 and Fig. 5 show the influence of α_f, f_{sw}, q_d and α_c on the frequencies f_{b+} and f_{b-}, i.e., their effect on the VSC negative-damping region. These VSC parameters are modified according to the range of values in Section 2.1.2. Moreover, Fig. 3, Fig. 4 and Fig. 5 allow the fair accuracy of (17) to be validated by comparing it with the PSCAD numerical results. The following conclusions (analytically justified in Section 3.2) can be drawn:

- The difference between negative- and positive-sequence frequencies is larger in normal operation mode (12) and for high values of f_{sw}.

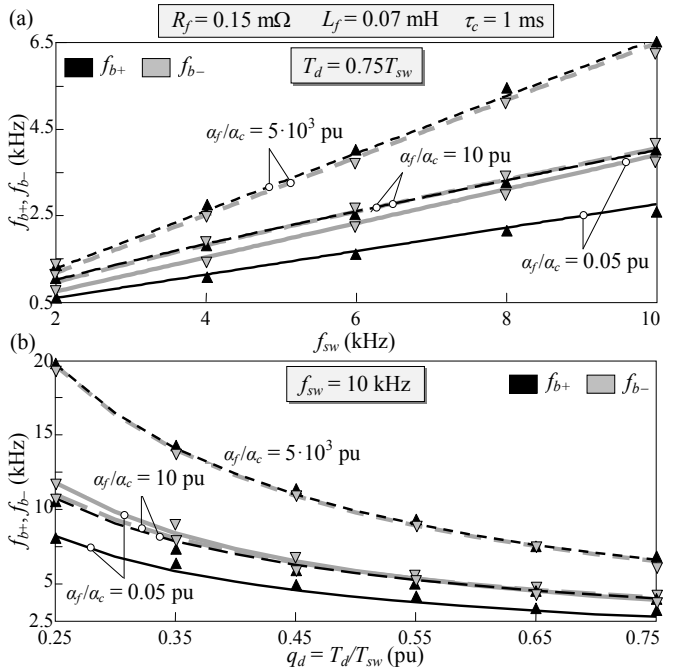

Fig. 4. *Influence of the VSC switching frequency* ***(a)*** *and the factor q_d* ***(b)*** *on the boundary frequencies f_{b+} and f_{b-} of the VSC negative damping region. Lines: Analytical expression (17); Dots: PSCAD results.*

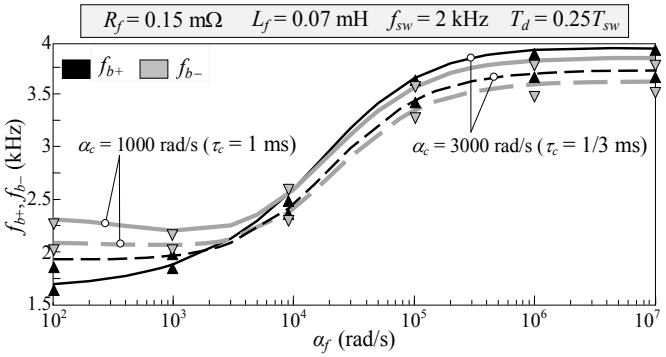

Fig. 5. *Influence of the CC bandwidth on the boundary frequencies f_{b+} and f_{b-} of the VSC negative damping region. Lines: Analytical expression (17); Dots: PSCAD results.*

- Large values of α_f shift the VSC non-negative damping region close to the VSC switching frequency (see Fig. 3).
- Frequencies f_{b+} and f_{b-} have approximately a direct proportionality to the VSC switching frequency (see Fig. 4(a)) and an inverse proportionality to the factor q_d, i.e., to the time delay T_d (9), (see Fig. 4(b)).
- The influence of the CC bandwidth α_c on f_{b+} and f_{b-} is smaller than that the other VSC parameters (see Fig. 5).

3.2. Approximations of the boundary frequencies

Approximate expressions of f_{b+} and f_{b-} are presented to better understand the influence of VSC parameters on the VSC negative-damping region. They are obtained from the numerator in (16) according to the value of α_f and considering the harmonic resonances in a frequency range where $|\omega| >> \omega_1$.

In normal mode, the numerator in (16) is simplified for small values of α_f as

$$G^N_{vsc\pm}(\omega) \approx D_{r\pm}\alpha_c\omega^2 - D_{i\pm}\omega^2\omega_1, \tag{18}$$

and the following analytical expressions of f_{b+} and f_{b-} are derived:

$$G^N_{vsc\pm}(\omega_{b\pm,n1}) \approx D_{r\pm}\alpha_c - D_{i\pm}\omega_1 = 0 \;\Rightarrow \begin{cases} f_{b+,n1} = \dfrac{\omega_{b+,n1}}{2\pi} = \dfrac{1}{2\pi}\dfrac{1}{T_d}\tan^{-1}\left(\alpha_c/\omega_1\right) \\ f_{b-,n1} = \dfrac{\omega_{b-,n1}}{2\pi} = \dfrac{1}{2T_d} - f_{b+,n1} \end{cases}. \tag{19}$$

For typical values of α_c (see Section 2.1.2), $\tan^{-1}(\alpha_c/\omega_1) \approx \pi/2$, and (18) is simplified by obtaining the following analytical expressions of f_{b+} and f_{b-} in normal mode:

$$G^N_{vsc}(\omega_{b\pm,n2}) \approx D_{r\pm}\alpha_c = 0 \;\Rightarrow\; f_{b\pm,n2} = \frac{\omega_{b\pm,n2}}{2\pi} = \frac{1}{4T_d}. \tag{20}$$

The above expression is commonly used in the literature to characterize the boundary frequency of the VSC negative damping region [4], [15], [17].

In transient mode, the numerator in (16) is simplified for large values of α_f as

$$G^N_{vsc\pm}(\omega) \approx (D_{r\pm} - 1)\alpha_f^2\alpha_c \pm D_{i\pm}\alpha_f^2\omega, \tag{21}$$

which, for typical values of α_c (see Section 2.1.2), is further simplified by obtaining the following analytical expressions of f_{b+} and f_{b-}:

$$\begin{aligned} &G^N_{vsc}(\omega_{b\pm,t2}) \approx D_{i\pm}\omega_{b\pm,t2} = 0 \\ &\Rightarrow \quad f_{b\pm,t2} = \frac{\omega_{b\pm,t2}}{2\pi} = \frac{1}{2T_d}. \end{aligned} \tag{22}$$

More accurate expressions of f_{b+} and f_{b-} are obtained if the terms $D_{r\pm}$ and $D_{i\pm}$ in (21) are approximated around $\omega = \omega_{b\pm,t2} = \pi/T_d$ (22) as $D_{r\pm} \approx -0.98$ and $D_{i\pm} \approx \pm(\pi - \omega T_d)$:

$$\begin{aligned} &G^N_{vsc}(\omega_{b\pm,t1}) \approx -1.98\alpha_c + (\pi - \omega_{b\pm,t1}T_d)\omega_{b\pm,t1} = 0 \\ &\Rightarrow \quad f_{b\pm,t1} = \frac{\omega_{b\pm,t1}}{2\pi} = \frac{1}{2\pi}\frac{\pi + \sqrt{\pi^2 - 7.92T_d\alpha_c}}{2T_d}. \end{aligned} \tag{23}$$

Comparing (22) and (23), it is observed that (22) is accurate only for small values of $T_d\alpha_c$, which leads to $7.92 \cdot T_d\alpha_c << \pi^2$ in (23).

Fig. 6 illustrates the errors between the different approximations of the frequency f_{b+} and those obtained from (17). Approximations (19) and (23) are accurate for determining f_{b+} in normal and transient operation mode with errors below 5%. Approximations (20) and (22) provide an initial estimation of f_{b+} but with high errors. The approximation in (22) could be used instead of (23) when the time delay is small, i.e., with high values of the VSC switching frequency and small values of the factor q_d, as shown in Fig. 6(b). These conclusions were numerically verified by comparing the different errors in the parameter range in Subsection 2.1.2, and can also be extended to the frequency f_{b-}.

3.3. Comments and recommendations on boundary frequencies and VSC parameter values

The approximate expressions in the previous Subsection clearly define the VSC negative-damping region and are used to analyze harmonic oscillatory instabilities. The system is stable if resonance frequencies f_r are lower than the boundary frequencies f_{b+} and f_{b-} since the VSC resistance is positive. Recommendations to determine the stability limits of VSC parameters can be derived from these approximate expressions. Moreover, these expressions validate the conclusions in Subsection 3.1 about the influence that VSC parameters on the VSC negative-damping region.

Boundary frequencies in normal operation mode (20) are approximately twice as high as in transient operation mode (22) (see Fig. 3). Therefore, according to (9), the positive-damping region may be extended by increasing α_f as follows:

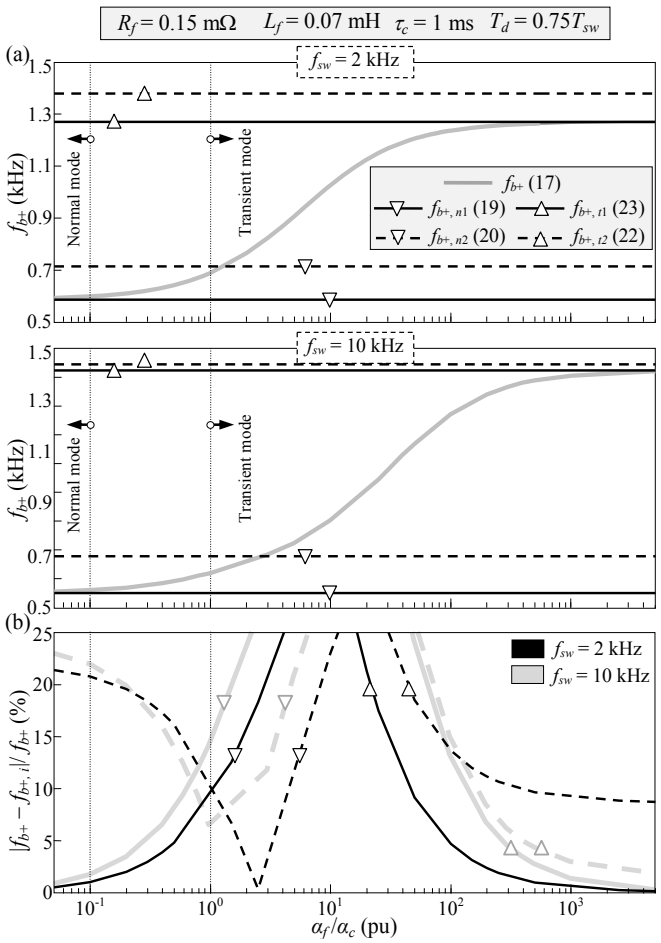

Fig. 6. *Approximations of the boundary frequency f_{b+}:*
(a) Boundary frequency. **(b)** Approximation errors.

- In the double-update PWM technique, from $1/(4T_d) = 1/(3 \cdot T_{sw}) = f_{sw}/3$ to $1/(2T_d) = 1/(1.5 \cdot T_{sw}) = f_{sw}/1.5$.
- In the single-update PWM technique, from $1/(4T_d) = 1/(2 \cdot T_{sw}) = f_{sw}/4$ to $1/(2T_d) = 1/(2 \cdot T_{sw}) = f_{sw}/2$.

Frequencies $f_{b\pm}$ in (19) and (22) are inversely proportional to time delay, i.e., they are proportional to the VSC switching frequency f_{sw} and inversely proportional to the factor q_d (see Fig. 4). According to this, the f_{sw} and q_d limits can be calculated to ensure that the boundary frequencies are above the harmonic resonance frequencies, preventing stability problems. In particular, (19) and (22)

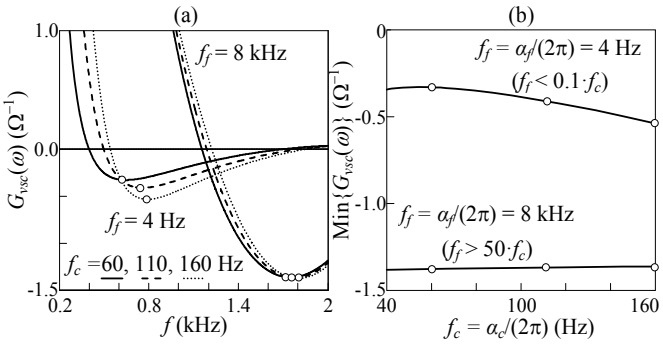

Fig. 7. *Influence of the CC bandwidth on the VSC conductance:*
(a) VSC conductance (16) plot. **(b)** Minimum values of the VSC conductance.

can be used to determine recommended values, f_{sw_rec} and q_{d_rec}, with a simple cross-multiplication:

$$f_{sw\_rec} = f_{sw}\frac{f_r}{f_b} \qquad q_{d\_rec} = q_d\frac{f_b}{f_r}. \tag{24}$$

It is observed that the VSC positive-damping region may be extended above the VSC switching frequency if q_d is reduced by reducing the CC computation time, as shown in Fig. 4(b). The VSC switching frequency f_{sw} is not a suitable parameter for reducing T_d because it affects CC design and VSC switching losses.

The influence of the CC bandwidth α_c on the boundary frequencies is small (see Fig. 5) because it depends on the factor $\tan^{-1}(\alpha_c/\omega_1)$ in normal operation mode and the factor $7.92\cdot T_d\alpha_c$ in transient mode, which do not have an important contribution in (19) and (23), respectively. Nevertheless, the CC bandwidth α_c may also affect the depth of the negative conductance (i.e., the minimum value of the negative conductance), worsening system stability. To analyze this, the VSC conductance in (16) can be approximated at harmonic resonance frequencies, $|\omega| >> \omega_1$, as

$$G_{vsc}(\pm\omega) \approx \begin{cases} \dfrac{D_{r\pm}\alpha_c - D_{i\pm}\omega_1}{L_f\omega^2} & \alpha_f < 0.1\alpha_c \\ \dfrac{D_{i\pm}\alpha_f^2}{L_f\omega(\omega^2+\alpha_f^2)} & \alpha_f > 50\alpha_c \end{cases}, \tag{25}$$

where it is observed that the CC bandwidth α_c affects the conductance $G_{vsc}(\pm\omega)$ in normal operation mode ($\alpha_f < 0.1\cdot\alpha_c$) but not in transient operation mode, with α_f greater than $50\cdot\alpha_c$. In normal mode, high values of α_c lead to high negative values of $D_{r\pm}\cdot\alpha_c$ for $f > f_{b\pm}$, increasing the depth of the negative conductance significantly, and therefore the risk of destabilization. The above conclusions are illustrated in Fig. 7, where the minimum values of $G_{vsc}(\omega)$ obtained from (16) in normal and transient operation mode and for different CC bandwidths are illustrated.

4. Applications

In order to show the paper's contribution, two applications, i.e., a traction system and an offshore WPP are presented.

4.1. Traction system

The 1x25 kV 50 Hz ac traction system in Fig. 8(a) is studied. Instability problems may appear as a result of the interaction between the VSC train and the traction system [7], [8]. To analyze these problems, the train fed by a VSC is modeled as its Norton equivalent circuit (5) and the traction system is characterized with the circuit in Fig. 8(b). The contact feeder section is represented by a distributed model dependent on train position with two concentrated parameter π-circuits at the left and right sides of the traction load [11] – [13]. Although distributed parameter π-circuits should be used to better assess traction system stability, the simple model used in the study is also considered in the literature [11] – [13] and allows the contribution of the paper to be easily discussed without losing generality. It must also be noted that the operating point of the VSC train is not used in the study because it does not affect the CC loop since the expressions characterizing this loop are linear, and must therefore not be linearized [2], [15].

The VSC admittance $Y_{vsc}(s)$ and the traction system equivalent admittance $Y_g(s)$ must be calculated. The VSC admittance is determined from (6) and the traction system equivalent admittance is obtained as follows:

$$Y_g(s) = \frac{1}{Z_{e1}(s)+Z_{TL}(s)} + \frac{1}{Z_f(s)} \qquad (0 < d < D), \tag{26}$$

where

$$Z_{e1}(s) = \left(\frac{1}{Z_{e2}(s)} + \frac{D}{2Z_C(s)} + \frac{D-d}{Z_L(s)(D-d)^2 + 2Z_C(s)}\right)^{-1}$$
$$Z_{e2}(s) = \frac{\left(Z_{TS}(s)+2Z_S(s)\right)2Z_C(s)/d}{Z_{TS}(s)+2Z_S(s)+2Z_C(s)/d} + Z_L(s)d, \tag{27}$$

where d is the distance between train location and the railroad substation.

The frequency response of the equivalent impedance magnitude $|\underline{Z}_t(\pm j\omega)| = |\underline{Y}_g(\pm j\omega) + \underline{Y}_{vsc}(\pm j\omega)|^{-1}$ $\omega > 0$ (7) with $\underline{Y}_{vsc}(\pm j\omega)$ in (15) is considered to recognize parallel resonances, and the damping $G(\pm j\omega) = \mathrm{Re}\{\underline{Y}_g(\pm j\omega) + \underline{Y}_{vsc}(\pm j\omega)\}$ $\omega > 0$ at these resonances is considered to analyze stability by the PND criterion. To assess system stability, this criterion must be verified for the positive- ($s = j\omega$) and negative- ($s = -j\omega$) sequence admittances. Traction system stability and VSC parameter

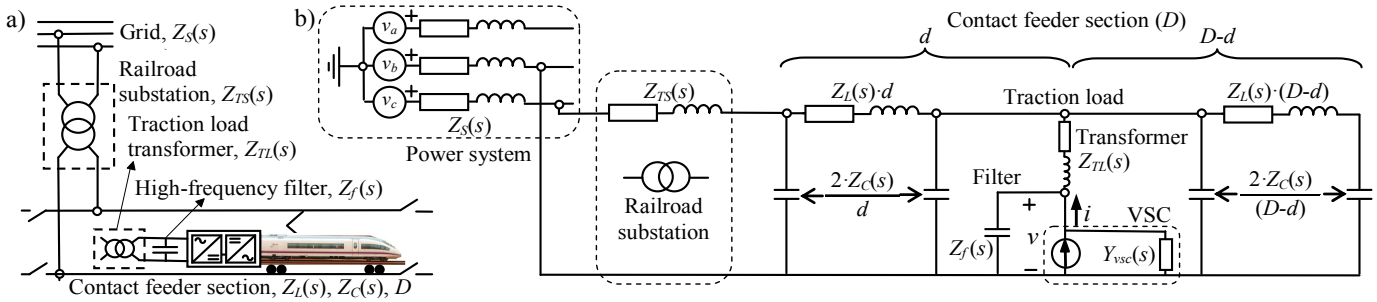

Fig. 8. *1x25 kV ac traction system:*
(a) Traction system installation. **(b)** Traction system circuit.

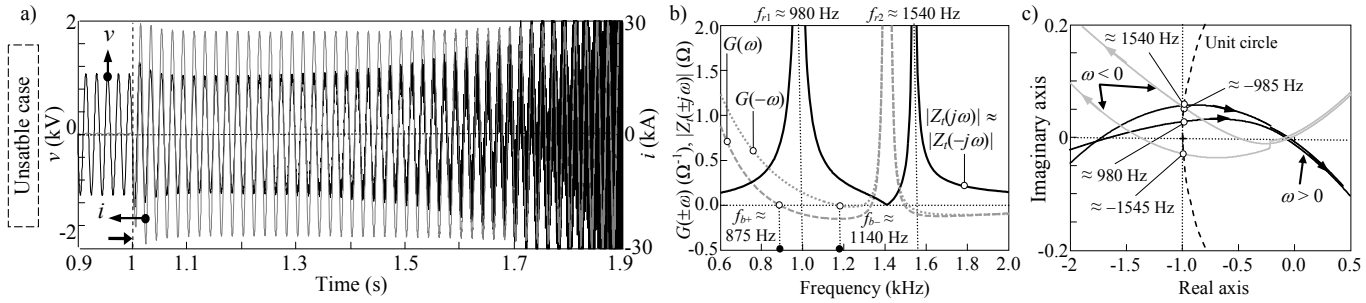

Fig. 9. *Unstable example (normal operation mode with $\alpha_f = 0.1\alpha_c$):*
(a) Time domain simulations of *v* and *i* at the VSC input. **(b)** Frequency plot of the equivalent impedance and damping factor. **(c)** Nyquist plot of the loop transfer function.

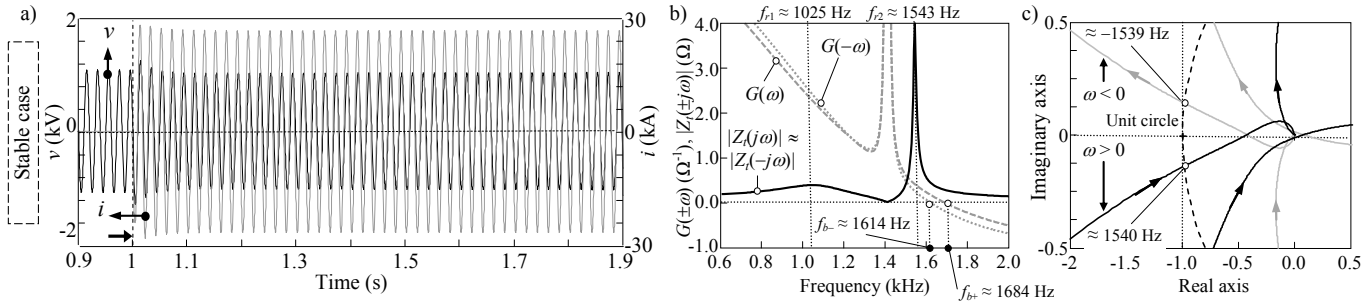

Fig. 10. *Stable example (transient operation mode with $\alpha_f = 25\alpha_c$):*
(a) Time domain simulations of *v* and *i* at the VSC input. **(b)** Frequency plot of the equivalent impedance and damping factor. **(c)** Nyquist plot of the loop transfer function.

recommendations are analyzed when the train is located at the beginning of the section ($d = 0.001$ km in (27)). The influence of train location on stability is subsequently determined.

Fig. 9 and Fig. 10 illustrate an unstable and a stable example depending on the grid voltage low-pass filter bandwidth α_f (normal operation mode with $\alpha_f = 0.1\alpha_c$ and transient operation mode with $\alpha_f = 25\alpha_c$, respectively). The other VSC control parameters are $\tau_c = 1/\alpha_c = 1$ ms, $T_d = 0.75 \cdot T_{sw}$ (double-update PWM technique) and $f_{sw} = 3$ kHz. The train is located at beginning of the section. PSCAD/EMTDC time-domain simulations for the train going in the section ($d = 0.001$ km in (27)) at instant 1s are plotted in Fig. 9(a) and Fig. 10(a). It is numerically verified from the simulations in Fig. 9(a) that the frequencies of the unstable oscillations are mainly located around 1550 Hz. The unstable example is anticipated by the PND criterion in Fig. 9(b) because the parallel resonance at f_{r1} is in the negative-damping region of $G(\omega)$ and the parallel resonance at f_{r2} is in the negative-damping region of $G(\pm\omega)$. The Nyquist plot for the positive- and negative-sequences of the loop transfer function $L(j\omega)$ $-\infty < \omega < \infty$ (8) in Fig. 9(c) confirms the results on instability. The Nyquist curve of the positive-sequence (black line) intersects the unit circle at 980 Hz and 1540 Hz, enclosing the −1 point in clockwise direction. The Nyquist curve of the negative-sequence (grey line) intersects the unit circle at −1545 Hz, enclosing the −1 point in clockwise direction. Note that the negative-sequence curve also intersects the unit circle at −985 Hz but does not encircle the −1 point, which corresponds to positive damping of $G(-\omega)$ at this frequency in Fig. 9(b). The stable example is anticipated by the PND criterion because the parallel resonances at f_{r1} (virtually damped) and f_{r2} are in the positive-damping region of $G(\pm\omega)$ in Fig. 10(b). The Nyquist plot of $L(j\omega)$ is in agreement with the results as the positive- and negative-sequence curves do not enclose the −1 point in Fig. 10(c). The results of these examples can be justified from the analysis in Section 3.

The damping region is modified with the values of α_f, f_{sw} and q_d to ensure system stability. The impact of these parameters on traction system stability is presented in Fig. 11, where α_f is modified from $0.1\alpha_c$ to $25\alpha_c$, f_{sw} from 3 to 8 kHz, q_d from 0.25 to 0.75 pu and $d = 0.001$ km in (27). Fig. 11 (left) plots the resonance frequencies f_{r1} and f_{r2} and the boundary frequencies f_{b+} and f_{b-}. The system is stable when the VSC parameter values shift f_{b+} and f_{b-} above the resonance frequencies f_{r1} and f_{r2} (grey area) because this ensures positive damping at the resonance frequencies. Fig. 11 (middle) shows the root locus of the poles associated with instability. The root locus of the poles illustrates that their imaginary part approximately matches the frequency of parallel resonances and their real part is related to system damping. The system is stable when all the poles are on the negative side of the real axis. If the boundary frequencies f_{b+} and f_{b-} shift to frequencies above the parallel resonances, the poles related to instability move to the negative side of the real axis. Fig. 11 (right) shows PSCAD/EMTDC time-domain simulations where contrast waveforms are provided for three values of the VSC parameters. Note that the traction system becomes stable or unstable according to VSC parameter values, a response predicted in the left and middle plots of Fig. 11, where simulation points are labeled. It can also be observed in Fig. 11 that for $\alpha_f = 25\alpha_c$ (example in Fig. 10) the resonance frequencies are in the stable region (grey area) and the real part of the poles is negative while this is not true for $\alpha_f = 0.1\alpha_c$ (example in Fig. 9).

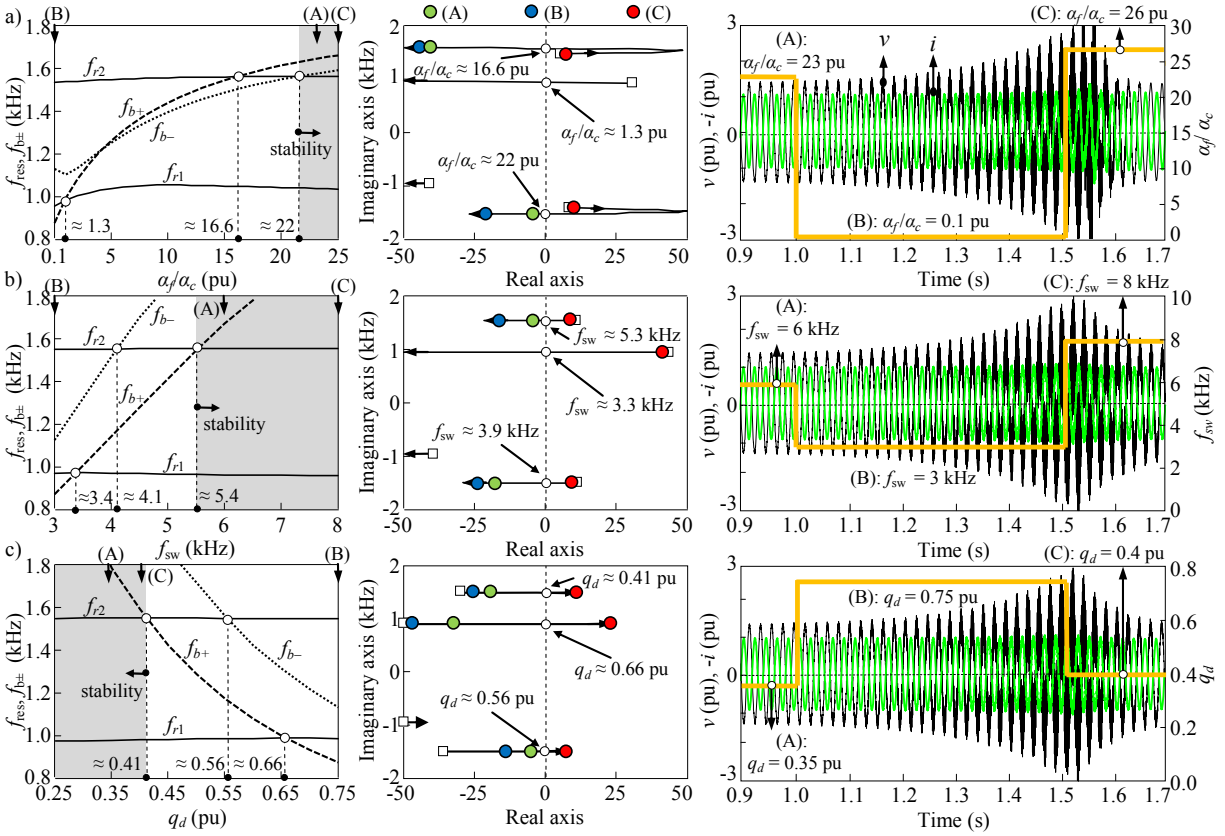

Fig. 11. *Influence of control parameter values on resonance and boundary frequencies (left), root locus of the poles (middle) and time domain simulations of the traction system (right):*
(a) Low-pass filter bandwidth. **(b)** Switching frequency. **(c)** Factor q_d.

The VSC parameter values ensuring system stability (see Fig. 11) are easily calculated by imposing that the boundary frequencies in (17) are higher than the resonance frequencies. The recommendations in Subsection 3.3 are also used to approximately determine these parameter values:

- Stability is ensured by increasing α_f because the positive-damping region is extended from $f_{sw}/3 \approx 1$ kHz to $f_{sw}/1.5 \approx 2$ kHz which is higher than the resonance frequency f_{r2}.
- According to (24), stability is ensured by decreasing q_d from 0.75 pu to $0.75 \cdot 875/1540 = 0.43$ pu and by increasing f_{sw} from 3 kHz to $3 \cdot 1540/875 = 5.28$ kHz. However, as pointed out in Section 3.3, the VSC switching frequency f_{sw} is not a suitable parameter for improving stability because it may affect other VSC variables and increase VSC losses.

In the previous studies, changes in traction system impedance and traction system stability due to train movement are not considered because the study is only focused on the analysis of the paper's contribution on the influence of VSC parameters on traction system stability. The impact of train location is analyzed below. It is numerically verified that the resonance frequencies of the traction system remain approximately unchanged but the impedance increases for greater distances between train location and the railroad substation. The influence of train location on stability is shown in Fig. 12, where the stability in the example in Fig. 10 is analyzed for all train locations from the beginning to the end of the section. PSCAD/EMTDC time-domain simulations in Fig. 12(a)

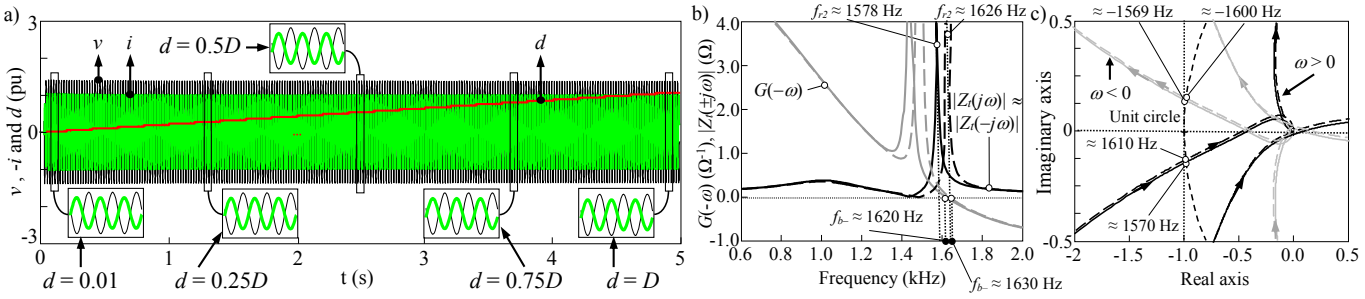

Fig. 12. *Influence of train location on system stability:*
(a) Time domain simulations of v and i at the VSC input. **(b)** Frequency plot of the equivalent impedance and damping factor ($d = 0.25$ in continuous line and $d = 0.75$ in dashed line). **(c)** Nyquist plot of the loop transfer function ($d = 0.25$ in continuous

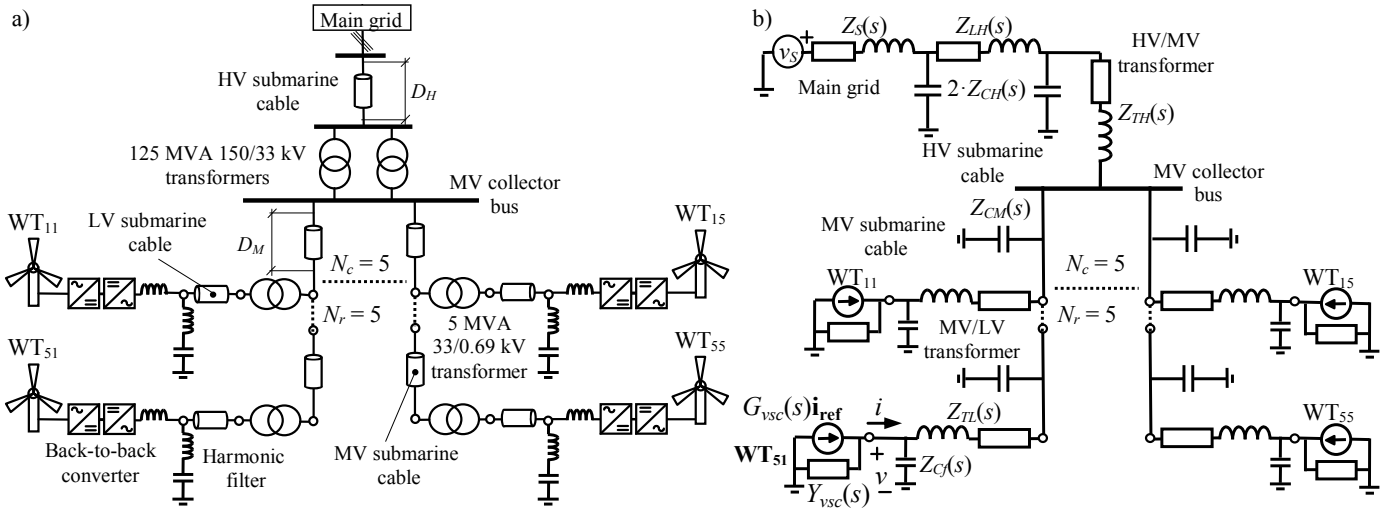

Fig. 13. *125 MW offshore WPP system:*
(a) WPP system installation. **(b)** WPP system circuit.

show that the traction system remains stable for any train location. Note that these simulations are made by assuming the contact feeder section to be covered by the train in 5 seconds. Obviously, this does not represent a real situation but allows the influence of train location on system stability to be analyzed from simulations without losing generality. Stability for $d = 0.25$ and 0.75 is predicted by the PND criterion in Fig. 12(b) because the parallel resonance at f_{r2} is in the positive-damping region of $G(-\omega)$, i.e., $f_{r2} = 1578$ Hz $< f_{b-} = 1620$ Hz for $d = 0.25$ and $f_{r2} = 1626$ Hz $< f_{b-} = 1630$ Hz for $d = 0.75$. Note that only the most critical conductance, i.e., $G(-\omega)$, is plotted in Fig. 12(b) for the sake of clarity. The Nyquist plot of $L(j\omega)$ in Fig. 12(c) verifies the results as the positive- and negative-sequence curves do not enclose the -1 point for any train locations. The same result is true for the other train locations. It is concluded in the example that train location does not affect system stability significantly. Fig. 12(b) also validates that the resonance frequency of the traction system remains approximately unchanged for $d = 0.25$ and 0.75 whereas the impedance increases.

4.2. Offshore wind power plant

The offshore WPP with 25 type-4 WTs in Fig. 13(a) is studied. The WTs, the collector system and the export system are at 0.69 kV, 33 kV and 150 kV, respectively. Filters are connected to Type-4 WT terminals to reduce frequency switching harmonics. Instability problems may appear as a result of the interaction between the converter control and the WPP. To analyze these problems, the WT VSCs are modeled as a Norton equivalent circuit (5) and the WPP is modeled with the circuit in Fig. 13(b). The submarine cables are represented as single concentrated parameter π-circuits because they are short enough to be well characterized for low frequencies. Moreover, the MV submarine cable model is approximated as the cable transversal capacitors because the longitudinal impedance is not significant compared with the transformer inductance. The LV submarine cables are not considered because their capacitors are very small and their impedance is included in the impedance of the transformer. The VSC filter capacitance of the WTs is considered in the study.

WPP stability is studied from WT_{51} (see Fig. 13(b)). The WT VSC equivalent admittance $Y_{vsc}(s)$ and the WPP equivalent admittance $Y_g(s)$ from the WT_{51} terminals must be determined. The VSC admittance is determined from (6) and the WPP equivalent admittance is calculated as follows:

$$Y_g(s) = \frac{Z_{Cf}(s) + Z_{TL}(s) + \dfrac{Z_{e1}(s)Z_{CM}(s)}{Z_{e1}(s) + Z_{CM}(s)}}{Z_{Cf}(s)\left(Z_{TL}(s) + \dfrac{Z_{e1}(s)Z_{CM}(s)}{Z_{e1}(s) + Z_{CM}(s)} \right)}, \tag{28}$$

where

$$\begin{aligned}
Z_{e1}(s) &= \left((N_r N_c - 1)\left(\frac{1}{Z_{CM}(s)} + \frac{1}{Z_{e2}(s)} \right) + \frac{1}{Z_{e3}(s)} \right)^{-1} \\
Z_{e2}(s) &= \frac{Z_{Cf}(s)/Y_{vsc}(s)}{Z_{Cf}(s) + 1/Y_{vsc}(s)} + Z_{TL}(s) \\
Z_{e3}(s) &= \frac{Z_{e4}(s)2Z_{CH}(s)}{Z_{e4}(s) + 2Z_{CH}(s)} + Z_{TH}(s) \\
Z_{e4}(s) &= \frac{Z_S(s)2Z_{CH}(s)}{Z_S(s) + 2Z_{CH}(s)} + Z_{LH}(s).
\end{aligned} \tag{29}$$

System stability is assessed by the same stability criteria as in the traction system application.

Fig. 14 and Fig. 15 illustrate an unstable and a stable example depending on the grid voltage low-pass filter bandwidth α_f (normal operation mode with $\alpha_f = 0.1\alpha_c$ and transient operation mode with $\alpha_f = 13.5\alpha_c$, respectively). The other VSC control parameters are $\tau_c = 1/\alpha_c = 1$ ms, $T_d = 0.75 \cdot T_{sw}$ (double-update PWM technique) and $f_{sw} = 3$ kHz. PSCAD/EMTDC time-domain simulations are plotted in Fig. 14(a) and Fig. 15(a), where the WT_{51} is connected at instant 1s. It is numerically verified from the simulations in Fig. 14(a) that the frequencies of the unstable oscillations are mainly located around 1350 Hz. Instability in Fig. 14(a) is predicted by the PND criterion in Fig. 14(b) because the parallel resonance at f_r is in the negative-damping region of $G(\pm\omega)$. The Nyquist plot of $L(j\omega)$ in

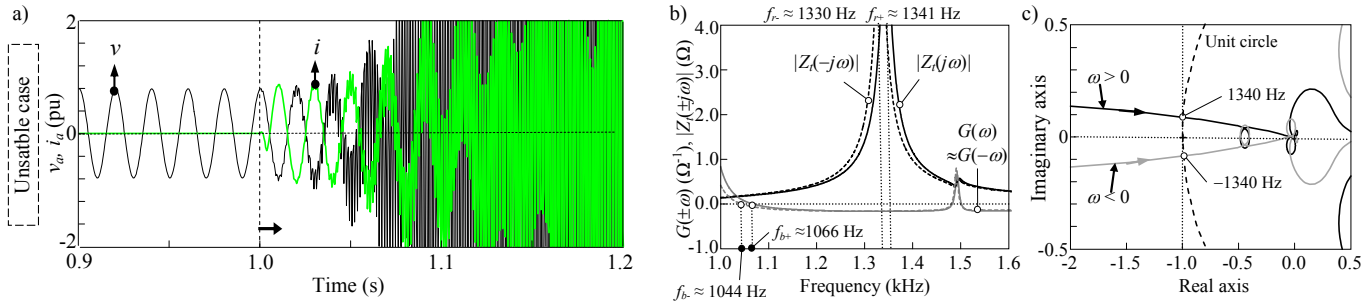

Fig. 14. *Unstable example (normal operation mode with $\alpha_f = 0.1\alpha_c$):*
(a) Time domain simulations of *v* and *i* at the VSC input. **(b)** Frequency plot of the equivalent impedance and damping factor. **(c)** Nyquist plot of the loop transfer function.

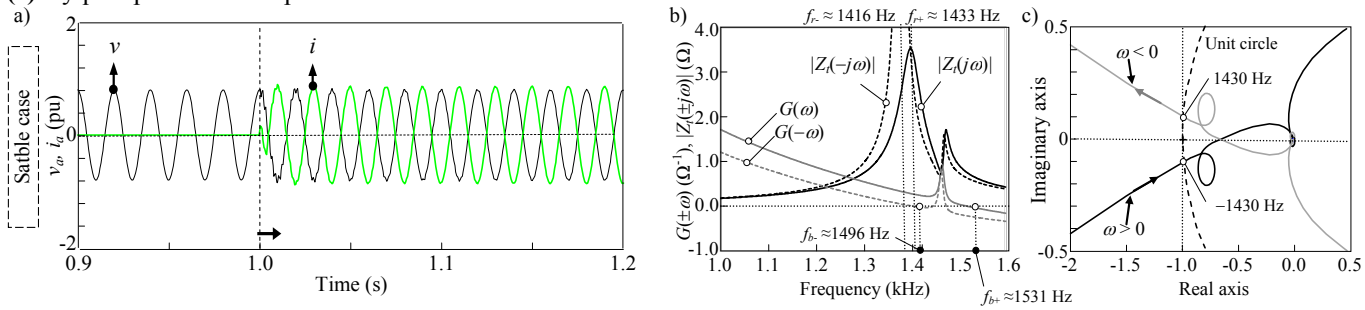

Fig. 15. *Stable example (transient operation mode with $\alpha_f = 13.5\alpha_c$):*
(a) Time domain simulations of *v* and *i* at the VSC input. **(b)** Frequency plot of the equivalent impedance and damping factor. **(c)** Nyquist plot of the loop transfer function.

Fig. 14(c) confirms the results because both the positive- and negative-sequence Nyquist curves enclose the −1 point in clockwise direction. Stability in Fig. 15(a) is predicted by the PND criterion in Fig. 15(b) because the parallel resonance at f_{r+} and f_{r-} is in the positive-damping region of $G(\pm\omega)$. The Nyquist plot of $L(j\omega)$ in Fig. 15(c) confirms the results because neither the positive- nor the negative-sequence Nyquist curves encloses the −1 point. It is worth noting that there is another parallel resonance in Fig. 14(b) and Fig. 15(b) but is not considered in the analysis because it is always in the positive-damping region of $G(\pm\omega)$.

The damping region is modified with the values of α_f, f_{sw} and q_d to ensure system stability. The impact of α_f and q_d on WPP stability is studied in Fig. 16, where α_f is modified from $0.1\alpha_c$ to $25\alpha_c$ and q_d from 0.25 to 0.75 pu. According to the comments about the switching frequency f_{sw} in the previous Sections, the influence of this parameter on stability is not determined. Fig. 16 (left) shows the plot of the resonance frequencies f_{r+} and f_{r-} and the boundary frequencies f_{b+} and f_{b-}. The system is stable in the grey area because this ensures positive damping at the resonance frequencies. Fig. 16 (middle) shows the root locus of the

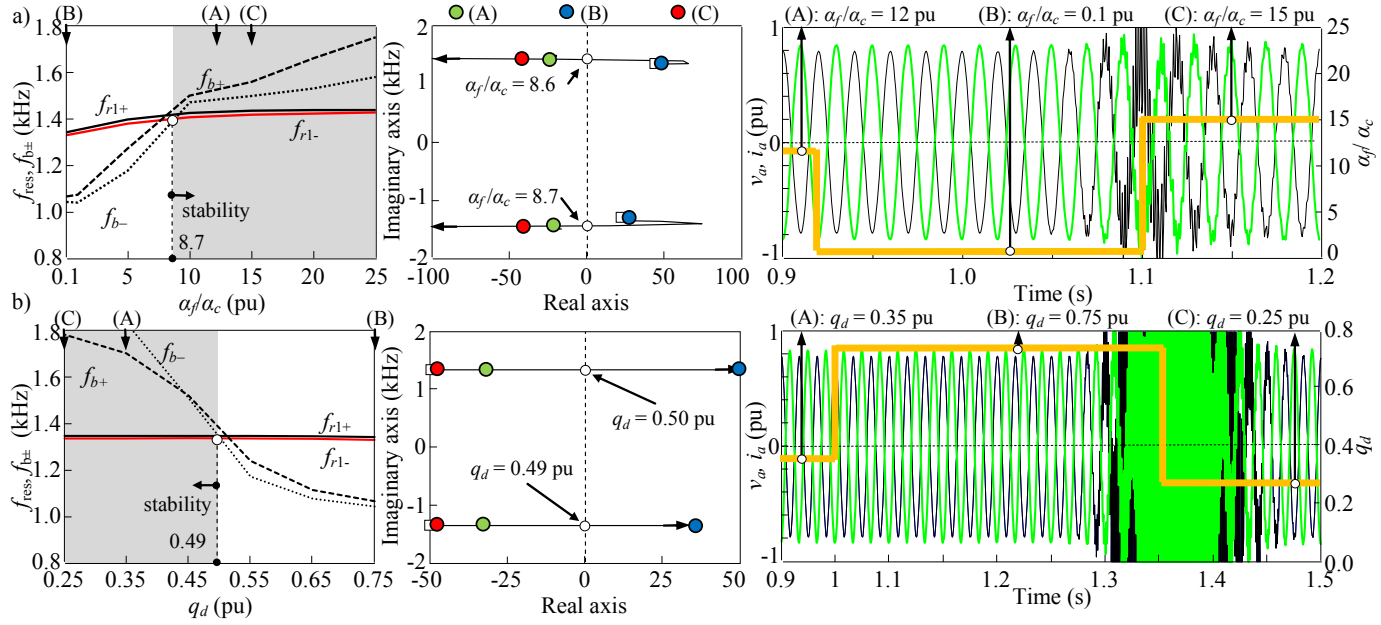

Fig. 16. *Influence of control parameter values on resonance and boundary frequencies (left), root locus of the poles (middle) and time domain simulations of traction system (right):*
(a) Low-pass filter bandwidth. **(b)** Factor q_d.

poles associated with instability. The root locus of the poles illustrates that their imaginary part approximately matches the frequency of parallel resonances and their real part is related to system damping. Note that, if the boundary frequencies f_{b+} and f_{b-} shift to frequencies above the parallel resonances, the poles related to stability move to the negative side of the real axis. Fig. 16 (right) shows PSCAD/EMTDC time-domain simulations where waveforms for three values of the VSC parameters are provided. It can be observed that the WPP becomes stable or unstable according to the values of the VSC parameters in the left and middle plots of Fig. 16. It can also be observed that for $\alpha_f = 13.5\alpha_c$ (example in Fig. 15) the resonance frequencies are in the stable region (grey area) and the real part of the poles is negative while this is not true for $\alpha_f = 0.1\alpha_c$ (example in Fig. 14).

The influence of the closed-loop CC bandwidth α_c is illustrated in Fig. 17, where $\tau_c = 1/\alpha_c$ is modified from 1 ms to 0.5 ms at instant 1s. The other VSC control parameters are the same as in the stable example in Fig. 15 (i.e., $\alpha_f = 13.5\alpha_c$, $T_d = 0.75 \cdot T_{sw}$ and $f_{sw} = 3$ kHz). PSCAD/EMTDC time-domain simulations in Fig. 17(a) show that WPP becomes unstable and this is predicted by the PND criterion and the Nyquist plot of $L(j\omega)$. It is numerically verified that the frequencies of the unstable oscillations approximately match the resonance frequencies. This example illustrates that the CC bandwidth α_c affects stability in normal operation mode and transient operation mode with ($\alpha_f < 50 \cdot \alpha_c$) because high values of α_c lead to high values of the VSC negative-damping region (see Fig. 7), increasing the risk of destabilization. This is not true in transient operation mode for α_f greater than $50 \cdot \alpha_c$.

5. Conclusions

This paper analyzes the influence of control parameters on the VSC damping region at harmonic resonance frequencies. Analytical expressions, validated with PSCAD simulations, are used to characterize the VSC negative damping region in normal and transient modes for the positive- and negative-sequence components. The study relates the boundary frequencies of the negative-damping region of the VSC admittance to the VSC parameters by simple but reliable analytical expressions. The study extends and clarifies the following existing findings about the VSC damping region:

- The main parameters to achieve VSC passivity are the bandwidth α_f and T_d (i.e., the switching frequency and the factor q_d) [4], [18], [22].
- The boundary frequencies of the negative-damping region in normal operation mode may double in transient operation mode [4].

As a contribution, recommendations are made to study harmonic oscillatory stability of grid-connected VSC systems:

- Boundary frequencies are proportional to VSC switching frequency and inversely proportional to time delay. Therefore, switching frequency and time delay could be accordingly used to increase the positive-damping region although the former is not recommended due to its influence on VSC design.
- If total time delay is reduced to PWM time delay (i.e., $T_d = 0.5T_s$), a positive conductance region may be obtained up to the Nyquist frequency $f_s/2$.
- Although the CC bandwidth α_c has a minor influence on f_{b+} and f_{b-}, it affects the depth of the negative conductance when $\alpha_f < 50\alpha_c$. The larger the α_c, the more negative the conductance (i.e., the higher the risk of destabilization). This is not true in VSC transient operation mode with $\alpha_f > 50\alpha_c$, where the influence of the CC bandwidth α_c on the depth of the negative conductance is not significant.

All these recommendations, as well as the proposed analytical expressions, allow the limits of VSC parameters to be obtained to ensure system stability. These limits can be compared with the design values of VSC parameters in order to evaluate the risk of system destabilization. Further changes in the values of these parameters could be proposed on the basis of the recommendations made in the paper.

6. Acknowledgments

This work was supported in part by the Ministerio de Ciencia, Innovación y Universidades (grant RTI2018-095720-B-C33); the Ministerio de Economía, Inndustria y Competitividad and the EU FEDER Funds (grant DPI2017-84503-R).

7. References

[1] Céspedes, M., Sun, J.: 'Impedance modelling and analysis of grid-connected voltage-source converters', IEEE Trans. on Power Syst., 2014, 29, (3), pp.1254-1261.

[2] Yazdani, A., Iravani, R.: 'Voltage-sourced converters in power systems. Modeling, control and applications': Hoboken, NJ, USA: Wiley, 2010.

[3] Buchhagen, C., Rauscher, C., Menze, A.: 'BornWin1 – First experiences with harmonic interactions in converter dominated grids', Proc. of the International ETG Congress June-Nov. 2015, pp. 27-33.

[4] Harnefors, L., Wang, X., Yepes, A. G., Blaabjerg, F.: 'Passivity-based stability assessment of grid-connected VSCs – An overview', IEEE Journal of Emerging and Selected Topics in Power Electronics, 2016, 4, (1), pp. 116–125.

[5] Stamatiou, G., Bongiorno, M.: 'Stability Analysis of Two-Terminal VSC-HVDC Systems using Net-Damping Criterion', IEEE Trans. on Power Delivery, 2016, 31, (4), pp. 1748-1756.

[6] Freijedo, F. D., Chaudhary, S. K., Teodorescu, R., Guerrero, J. M., Bak, C. L., Kocewiak, L. H., Jensen, C. F.: 'Harmonic resonances in wind power plants: modeling, analysis and active mitigation methods', Proc. of the IEEE PowerTech, Eindhoven, June-July 2015, pp. 1-6.

[7] Möllerstedt, E., Bernhardsson, B.: 'Out of control because of harmonics–An analysis of the harmonic response of an inverter locomotive', IEEE Control Systems Magazine, 2000, 20, (4), pp. 70-81.

[8] Paice, A., Mayer, M.: 'Rail network modelling and stability: The input admittance criterion', Proc. 14th Int. Symp. Math. Theory Network Systems, Perpignan, France, June 2000, [CD-ROM].

[9] Bahrani, B.: 'Advanced control strategies for voltage source converters in microgrids and traction networks', Ph.D. Dissertation, Faculté des Sciences et Techniques de L'Ingénieur, Laboratorie D'Électronique Industrielle, Programme Doctoral en Energie, École Polytechnique Fédérale Lausanne, Switzerland, 2011. [Online]. Available: http://infoscience.epfl.ch/record/181221/files/EPFL_TH5479.pdf.

[10] Aeberhard, M., Meyer, M., Courtois, C.: 'The new standard EN 50388-2, Part 2—Stability and harmonics', Elektrische Bahnen, 2014, 12, (1), pp. 28-35.

[11] Kolar, V. et al.: 'Interference between electric traction supply network and distribution power network – Resonance phenomenon', Proc. 14th IEEE Int. Conference on Harmonics and Quality of Power, 2010, pp. 1-4.

[12] Guo, L., Li, Q., Xu, Y.: 'Study on harmonic resonance of traction line in electrified high-speed traction system', Proc. of the Int. Conference on Sustainable Power Generation and Supply (SUPERGEN), 2009, pp. 1-4.

[13] Tan, P-C., Chiang, P., Grahame, D.: 'A robust multilevel hybrid compensation system for 5-kV electrified railway applications', IEEE Trans. on Power Delivery, 2004, 19, (4), pp. 1043-1052, 2004.

[14] Sainz, L., Cheah-Mane, M., Monjo, Ll., Liang, J., Gomis-Bellmunt, O.: 'Positive-net-damping stability criterion in grid-connected VSC systems', IEEE Journal of Emerging and Selected Topics in Power Electronics, 2017, 5, (4), pp. 1499–1512.

[15] Harnefors, L., Bongiorno, M., Lundberg, S.: 'Input-admittance calculation and shaping for controlled voltage-source converters', IEEE Trans. on Industrial Electronics, 2007, 54, (6), pp. 3323-3334.

[16] Harnefors, L., Zhang, L., Bongiorno, M.: 'Frequency-domain passivity-based current controller design', IET Power Electronics, 2008, 1, (4), pp. 455-465.

[17] Harnefors, L., Yepes, A. G., Vidal, A., Doval-Gandoy, J.: 'Passivity-based controller design of grid-connected VSCs for prevention of electrical resonance instability', IEEE Transactions on Industrial Electronics, 2015, 62, (2), pp. 702-710.

[18] Harnefors, L., Finger, R., Wang, X., Bai, H., Blaabjerg, F.: 'VSC input-admittance modeling and analysis above the Nyquist frequency for passivity-based stability assessment', IEEE Transactions on Power Electronics, 2017, 64, (8), pp. 6362-6370.

[19] Sun, J.: 'Impedance-based stability criterion for grid-connected inverters', IEEE Transactions on Power Electronics, 2011, 26, (11), pp. 3075-3078.

[20] Harnefors, L.: 'Proof and application of the positive-net-damping stability criterion', IEEE Transactions on Power Electronics, 2011, 26, (1), pp. 481-482.

[21] Zhao, M., Yuang, X., Hu, J., Yan, Y.: 'Voltage dynamics of current control time-scale in a VSC-connected weak grid', IEEE Transactions on Power Systems, 2016, 31, (4), pp. 2925-2937.

[22] Céspedes, M., Sun, J.: 'Mitigation of inverter-grid harmonic resonance by narrow-band damping', IEEE Journal of Emerging and Selected Topics in Power Electronics, 2014, 2, (4), pp. 1024-1031.

[23] Céspedes, M., Sun, J.: 'Impedance shaping of three-phase grid parallel voltage-source converters', Proc. of the IEEE APEC, Feb. 2012, pp. 754-760.

[24] Wang, L., Blaabjerg, F., Loh, P. C.: 'Grid-current-feedback active damping for LCL resonance in grid-connected voltage-source converters', IEEE Transactions on Power Electronics, 2016, 31, (1), pp. 213-223.

[25] Jiang, Y., Lindberg, J., Lundberg, P., Svensson, J., Palsson, R.: 'Electric power converter', Patent EP 1 717 941 A2, ABB Technology AG, Nov. 2006.

8. Appendix: Positive-net-damping criterion

The impedance-based stability criterion can be reformulated to include net damping evaluation at harmonic resonances of the grid-connected VSC system as stability criterion instead of the phase margin [11]. For the sake of simplicity, this reformulation is presented considering only the positive-sequence (i.e., $s = j\omega,\ \omega > 0$) but the conclusions must also be applied for the negative-sequence. Considering the frequency response of the grid and the VSC admittances in Fig. 1(b) as follows:

$$Y_i(j\omega) = \left|Y_i(j\omega)\right| e^{\phi_i(j\omega)} = G_i(\omega) + jB_i(\omega) \quad (i = g, vsc), \quad (30)$$

the intersection of the grid and VSC admittance magnitudes $|Y_g(j\omega)| = |Y_{vsc}(j\omega)|$ is expressed as

$$G_g^2(\omega) + B_g^2(\omega) = G_{vsc}^2(\omega) + B_{vsc}^2(\omega). \quad (31)$$

The resistive components in ac grids and VSCs may usually be neglected compared to the reactive components (i.e., $G_i(\omega) << B_i(\omega)$ for $i = vsc, g$) [11] and (31) can be simplified to

$$B_g(\omega) \approx \pm B_{vsc}(\omega), \quad (32)$$

where the expression with the negative sign in (32) corresponds to the condition of the parallel resonance observed from the VSC current source in Fig. 1(b), i.e.,

$$\mathrm{Im}\left\{Y_g(j\omega)+Y_{vsc}(j\omega)\right\}\approx 0 \quad \Rightarrow \quad B_g(\omega)\approx -B_{vsc}(\omega). \tag{33}$$

The net damping of the grid-connected system $G(\omega) = G_g(\omega) + G_{vsc}(\omega) = \mathrm{Re}\{Y_g(j\omega) + Y_{vsc}(j\omega)\}$ can be expressed as

$$G(\omega)=\left|Y_g(j\omega)\right|\cos(\phi_g(j\omega))+\left|Y_{vsc}(j\omega)\right|\cos(\phi_{vsc}(j\omega)). \tag{34}$$

Considering the phase margin of the system $\phi_m = \pi - (\phi_{vsc}(j\omega) - \phi_g(j\omega))$ at the frequencies where $|Y_g(j\omega)| = |Y_{vsc}(j\omega)|$, (34) can be rewritten as

$$\begin{aligned} G(\omega) &= \left|Y_g(j\omega)\right|\left(\cos(\phi_m+\phi_{vsc}(j\omega)-\pi)+\cos(\phi_{vsc}(j\omega))\right) \\ &= \left|Y_g(j\omega)\right|\left(\cos(\phi_{vsc}(j\omega))-\cos(\phi_m+\phi_{vsc}(j\omega))\right). \end{aligned} \tag{35}$$

The stability condition $\phi_m > 0$ implies that $\cos(\phi_{vsc}(j\omega)) > \cos(\phi_m + \phi_{vsc}(j\omega))$, and (35) leads to the following net damping stability condition at these frequencies:

$$G(\omega)=G_g(\omega)+G_{vsc}(\omega)>0. \tag{36}$$

The PND criterion asserts that net damping at harmonic resonance frequencies of the system must be positive to ensure stability [11]. In grid-connected VSC systems, grid resistances are usually small and stability may be approximately studied from VSC damping because $G(\omega) \approx G_{vsc}(\omega)$.